Data rich imaging approaches assessing fatigue crack initiation and early propagation in a DS superalloy at room temperature

Y.G. Tan[a,*], D.J. Bull[a], R. Jiang[b], A. Evangelou[a], S. Chaudhuri[a], S. Octaviani[a], F. Pierron[a], N. Gao[a], H. Toda[c], I. Sinclair[a], P.A.S. Reed[a]

[a] Department of Mechanical Engineering, Faculty of Engineering and Physic Science, University of Southampton, Southampton SO17 1BJ, UK

[b] College of Energy and Power Engineering, Nanjing University of Aeronautics and Astronautics, Nanjing, China, 210016

[c] Department of Mechanical Engineering, Kyushu University, 744, Motooka, Nishi Ward, Fukuoka 819-0395, Japan

Abstract

Crack initiation and early propagation behavior of the directionally solidified (DS) superalloy CM247LC has been assessed by data rich imaging approaches. These include conventional characterization methods such as replica record analysis, 3D optical surface imaging, optical and scanning electron microscopy (SEM) as well as more recent techniques like digital image correlation (DIC) and synchrotron radiation computed tomography (SRCT). Three modes of secondary crack behaviors were found during evaluation of the fatigue process. The early stages of fatigue damage were controlled by microstructure-induced cracking, mainly consisting of carbide cracking. Fatigue damage was then promoted via slip band cracking and opening mode controlled carbide-cracking. The mechanisms of these different cracking behaviors are associated with the plastic zone of the main crack tip. Even though the early localized strain levels were of the same intensity within slip bands and at the intersection sites with carbides, carbide-induced cracking occurred prior to slip band cracking, characterized by SEM-DIC. This indicated that carbide-induced cracking was more likely to occur in the early stages of the fatigue process. Early crack growth behaviors were further investigated *in situ* at the microstructural scale via SRCT. The effect of carbides on crack initiation and propagation processes were evaluated in 3D. This revealed the phenomenon around pores, that cracks simultaneously grew on different slip planes in 3D, contrary to previous theories that such cracks tend to grow on a single favorable slip plane (in polycrystalline alloys). The SRCT result demonstrates the importance and necessities of 3D characterization of the crack propagation behavior at sub-surface, which is hardly analyzed by 2D characterization.

Key Words: Directionally solidified Ni-based superalloy; fatigue crack initiation; Short crack; digital image correlation; Synchrotron radiation computed tomography

1. Introduction

Fatigue damage is one of the most serious problems limiting service life of Ni-based superalloys. These materials are widely used in aeroengine and power generation turbomachinery, experiencing extremes of temperature and cyclic loading conditions[1-4]. To optimize fatigue resistance and prolong the service life of Ni-based superalloys, numerous studies have been conducted on mechanisms of fatigue crack initiation and early growth behaviors [5-16]. It is commonly accepted that fatigue cracks are very sensitive to microstructural features at room temperature. For instance, non-metallic inclusions (such as carbides and nitrides), grain boundaries (GBs) and twin boundaries (TBs) are thought to be crack initiation sites in polycrystal superalloys [17-20]. Dislocations are usually blocked and pile up close to these microstructure barriers, leading to local stress/strain concentration. In addition, early crack propagation is also associated with these microstructural features. Planar slip is more likely to be induced in coarse grains with less GB barriers compared to fine grains, giving rise to more evident faceted crack morphologies [7, 21]. In single crystal superalloys, crack initiation and early propagation behaviors are mainly influenced by precipitates and defects [16, 22]. Firstly, precipitates and defects, depending on their size, location and shape [23], can act as stress/strain concentrators, which can cause cracks to initiate. Secondly, these micro-features usually influence dislocation slip behaviors, *e.g.* the dislocation-precipitate cutting mechanism is activated in the regions of fine γ′, causing planar slip, while a dislocation-precipitation bowing mechanism is activated in regions of coarse γ′, leading to less planar slip [15]. Planar slip usually induces locally straight crack paths and higher crack growth rate. In contrast, less planar slip leads to deflected cracks and lower crack growth rate. CM247LC superalloy is the latest development of the first-generation directionally solidified (DS) superalloys, and is showing good performance under extreme temperatures and complex stress states[24, 25]. The alloy possess some microstructural characteristics of both polycrystal and single crystal superalloys. The large-size columnar grains [15], straight grain boundaries (GBs), carbides [26] and defects all could influence crack initiation and early propagation behavior. As a result, the mechanism of early crack growth could be very complicated, and effectively extend over much of a DS component's lifetime. Understanding this mechanism requires assessing the contribution of each factor to fatigue damage development in the alloy, thus requiring both conventional characterization methods, including surface replicas, optical microscopy (OM), scanning electronic microscopy

(SEM), as well as advanced characterization techniques such as SEM-DIC and Synchrotron radiation computed tomography (SRCT).

Digital image correlation (DIC) on Scanning Electon Microscopy (SEM) images is able to provide full-field strain distributions at a sub-micron scale, by correlating a random speckle pattern between reference and deformed images. Because crack initiation behavior is closely related to the strain localization/distribution at microstructural features, this technique has been employed widely in studying early crack growth behaviors [7, 27-29]. Stinville *et al.* [21] found that the strain is mainly accumulated within slip bands adjacent and parallel to twin boundaries (TBs) via this technique, confirming that TBs enhance the strain localization. Texier *et al.* [30] utilize the high resolution (HR) DIC to study the crack initiation behavior at non-metallic inclusions (NMI), *i.e.* carbides or nitrides in a polycrystalline superalloys. They found that the crack initiation could be assisted by slip localization, especially when intense strain localization along a TB intercepts the NMI. Wael *et al.* [27] studied the plastic strain accumulation and dislocation interaction at GBs via combining a DIC technique with molecular dynamic (MD) simulations. It is revealed that strain localization at the vicinity of GBs is increased with the magnitude of the residual Burgers vectors ($|b_r|$) of dislocations. The magnitude of $|b_r|$ is associated with misalignment of the slip systems in neighboring grains. Larger misalignment is less favored in dislocation transmission across GBs, leading to a high magnitude of residual Burgers vector and strain accumulation. The work explicitly explain the mechanism that high misoriented neighboring grains favor crack initiation at GBs, while crack transmission is promoted by less misoriented neighboring grains. Jiang *et al.* [7] combined DIC with electron backscatter diffraction (EBSD) in their research on a polycrystal superalloy, and developed a new fracture criterion for future crystal plastic finite element (CPFE) models. The transverse strain ε_{yy} measured by DIC and the inclination angle θ (between dislocation slip direction and activated slip trace on {111} planes) were identified as two indicators determining development of out-of-plane and in-plane cracks. Moreover, DIC measurement was used in characterizing the strain localization process around pores of different sizes and shapes [23]. It was found that larger sized pores with a sharp tip or local ‘ridge’ could be more effective stress concentrators and cause crack initiation. All these research studies show that DIC is a promising tool for understanding the very localized strain accumulation and crack initiation mechanisms in such systems.

The aforementioned measurements are two-dimensional (2D), providing information only on the surface fatigue crack behaviors. However, in reality cracks initiate and extend in three directions under triaxial stress states [31]. The dimension normal to the surface cannot be captured by surface based 2D characterization tools. As a result, some bias in understanding the fatigue cracking mechanism might be brought in. To overcome the disadvantages of 2D assessment, 3D techniques are employed. Widely used 3D characterizations include metallography serial sectioning, FIB milling

and X-ray computed tomography (X-ray CT) [7, 15, 32, 33]. For the destructive methods (metallography serial sectioning/FIB milling) the observed crack growth behavior is highly dependent on the selected regions/planes of observation. X-ray CT and SRCT are both non-destructive tools and capable of reconstructing the three dimensional representations of the area of interest (AOIs) at sub-micron scale [15, 22, 32, 34]. Meanwhile, the acquisition time of projection images via SRCT is much reduced compared to traditional X-ray computed tomography (CT), facilitating *in situ* observation of the damage evolution in the bulk. Thus, this technique can provide an unambiguous insight into historically inaccessible cracking processes at the microstructure-length scale [35, 36]. Morgeneyer *et al.* [31] combined this technique with digital volumetric correlation (DVC) to investigate early formation of slant fracture. The research confirmed that strain localization at the slant bands is at the origin of slant ductile fracture, and revealed the process of crack formation in 3D. In addition, SRCT can provide accurate quantification of microstructure features, such as the size, locations and shapes of larger secondary phases, as well as defects and grains. Hassanipour *et al.* [37] ranked the contribution of microstructural features to crack growth behavior, by utilizing the quantification offered by SRCT combined with global sensitivity and principal component analysis.

The main aim of the present work is to provide a well-rounded and deep understanding of fatigue crack initiation and early propagation mechanism in a DS superalloy CM247LC at low temperatures, by combining traditionally well-established and recently emerging characterization techniques. Replica record analysis, Alicona confocal microscope, OM and SEM were utilized to capture the interaction between cracks and GBs, secondary phases and defects. SEM-DIC was employed to further analyze the strain localization process at these microstructure features. SRCT was carried out to provide an in-situ observation of crack evolution at the microstructural scale. This 3D observation is compared to the 2D observations and reveals a better understanding of fatigue cracking mechanisms in this system.

2. Material and Experimental Procedures

2.1 Material and Microstructure Characterization

The CM247LC DS superalloy used in present work was provided by GE Power. The composition (in wt.%) of the alloy is listed in Table 1. This DS alloy was provided in the form of a block with the longest dimension in the solidified direction (<100> direction). Subsequently, the block was solution heat-treated at 1221 ^{o}C, 1232 ^{o}C, 1246 ^{o}C, respectively, followed by dual aging heat treatments at 1080 ^{o}C and 870 ^{o}C. Cubic specimens with a size of 10 × 10 × 10 mm^3 were extracted from the center of the block for microstructure characterization.

Table 1 Composition of CM247LC alloy (in wt. %)

Cr	Co	Al	Ti	W	Mo	Ta	Hf	C	Zr	B	Ni
8.25	9.23	5.31	0.75	9.50	0.51	3.20	1.46	0.75	<0.02	<0.02	Bal

Both surfaces parallel and perpendicular to the <100> solidification direction were ground, polished and etched in Kalling's reagent (40 g $CuCl_2$ + 80 ml HCl + 40 ml CH_3OH) for 10 – 20 s, to reveal the morphology of dendrites, grain boundaries and precipitates. Electro-etching was conducted in a solution of 10% orthophosphoric acid in H_2O at a voltage of 2 V for 25 s to reveal secondary and tertiary γ′. The microstructural features were observed by an Olympus BH2 OM and a JEOL JSM 6500F field emission gun (FEG) SEM (imaging parameters are shown in Table 2). The element analysis was performed using Energy Dispersive Spectrometer (EDS) attached to the SEM.

2.2 Fatigue Test

Two types of specimens were prepared for fatigue testing, i.e. plain bend bars (PBB) and dog-bone bars. The PBB specimens were used to assess the crack initiation and propagation behavior at different stages of the fatigue process. Dog-bone specimens were used for strain localization characterization and SRCT scanning, because their narrow gauge section facilitated these two kinds of characterization. The dimensions of the PBB and dog-bone specimens are shown in Figs. 1(a) and (b) and the specimens were extracted by electrical discharge machining (EDM).

Three-point bending fatigue tests were conducted on PBB specimens on an Instron 8501 hydraulic testing machine with a 20 Hz sine waveform and a load ratio of 0.1 at room temperature. The loading direction is perpendicular to the columnar grains of specimens as shown schematically in Fig. 1(a). When setting up the PBB specimen loading configuration, the distance between the two rollers on the top surface is 40 mm, while a roller is located at the bottom at the midpoint. The applied load was chosen to produce a maximum total stress equal to 95% of the yield stress on the top central surface, calculated using simple elastic beam theory. A replica technique on a sequentially interrupted test was utilized to monitor crack evolution on the surface. Replicas were firstly made at the top surface at intervals of every 5000 cycles until crack initiation, then at intervals of every 1000 cycles to observe the early crack propagation. The fracture surfaces were observed by Alicona confocal microscope and the JEOL FEG SEM JSM6500 machine.

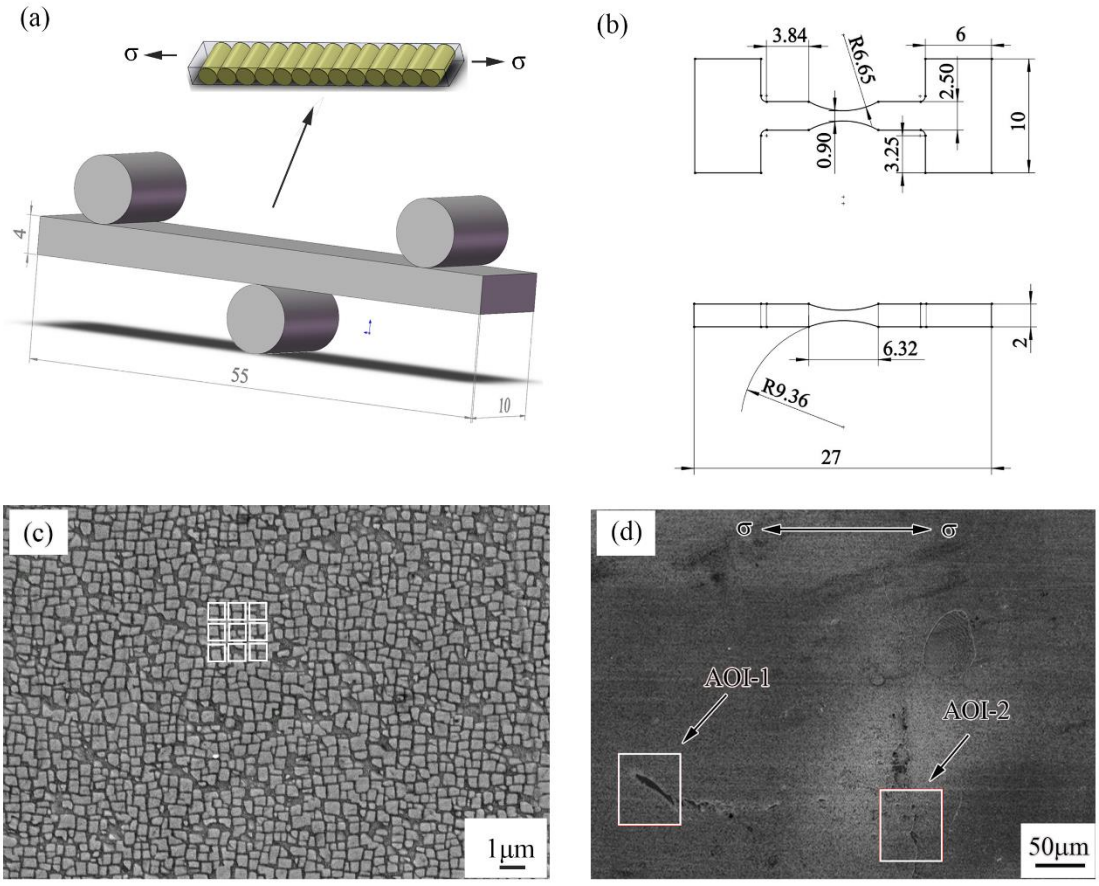

Figure 1 Schematic diagram of (a) PPB (the cylinders inside the cuboid represent the columnar grains) and (b) dog-bone specimens; all dimensions are displayed in mm; (c) speckle patterns; (d) area of interest for DIC analysis.

The dog-bone specimens were ground with 4000 grit, polished and etched in Kalling's solution to reveal the γ/γ′ microstructure as speckle patterns for subsequent SEM-DIC (shown in Fig. 1 (c) with subsets indicated). Reference images were taken at the gauge section by SEM under secondary electron imaging (SEI) mode and stitched together via Image J before fatigue testing commenced. The imaging parameters are shown in Table 2, following guidelines proposed by the literature [7]. Tension-tension fatigue tests were carried out on these specimens on an Instron Electropuls testing machine with a 20 Hz sine waveform and a load ratio of 0.1 at room temperature. Loading direction is perpendicular to the primary dendrite direction of the specimens. A load was applied to produce a maximum nominal stress of ~ 85% yield stress at the narrowest cross-section of the gauge. The tests were interrupted at 10000, 15000 and 22700 cycles to obtain SEM images at the deformed gauge section.

Table 2 Imaging parameters in JEOL SEM JSM6500F

Imaging mode	Acceleration voltage	Probe current spot size	Imaging time	Working distance	Strain field	Pixel size
SEI	15 keV	13	80 s	9.9 mm	600 × 600 μm^2	38 nm/pixel

2.3 *Ex situ* SEM-DIC Characterization

DIC analysis of the strain localization in the gauge section of the dog-bone specimens was conducted via MatchID commercial software. A subset of 21 × 21 pixels (0.798 µm × 0.798 µm) and a step size of 7 pixels were used. This is a compromise between larger step sizes which are computationally efficient and smaller ones which capture the local strain peaks more accurately. The zero-normalized sum of squared differences (ZNSSD) criterion, which accounts for offset and scaling in intensity variations of the investigated images, was adopted to perform the correlation in order to exclude the effects of contrast difference in the SEM images taken at different observation times. Deformed images were interpolated using bicubic splines to obtain subpixel accuracies in the displacement calculation. Quadratic shape functions were used to expand the displacement field in the subset. This is a better choice than linear shape functions, as demonstrated in [38] and leads to enhanced spatial resolution. Once the displacement field was calculated, the Logarithmic Euler-Almansi strain fields were derived by performing a local bilinear polynomial fit in MatchID using a window of 3 x 3 data points (or a 'strain window' of 3). The smallest possible strain window was selected here to enhance spatial resolution at the cost of strain resolution. Due to the *ex situ* nature of SEM-DIC, a noise sensitivity study was performed and the details of the noise assessment can be found in a previous publication [7].

A full-field strain map was measured in a region containing two columnar grains shown in Fig. 1(d). Strain components were calculated and transformed into local coordinates associated with the maximum shear strain in the left columnar grain. Two AOIs were selected from the stitched image for further analysis, shown in Fig. 1(d). AOI-1 is a carbide within grains, while AOI-2 is a carbide at a grain boundary. To simplify the comparison of strain bands of different orientations, maximum shear strains in each DIC characterization were calculated using following equation. This is the radius of Mohr's circle and is independent of the coordinate system.

$$\varepsilon_{xy}^{max} = \sqrt{(\frac{\varepsilon_{xx}-\varepsilon_{yy}}{2})^2 + \varepsilon_{xy}^2} \quad (1)$$

Table 3 Parameters for DIC analysis

DIC software	MatchID
Correlation alogorithm	ZNSSD
Interpolation	Bicubic spline
Shape functions	Quadratic
Pre-smoothing	Gaussian 5
Subset	21 pixels
Step size	7 pixels
Strain window	3 data points
Virtual strain gauge size	35 pixels

2.4 *In situ* SRCT Characterization

The *in situ* SRCT characterization was conducted at Spring-8, Japan. The selected dog bone geometry was aligned with primary dendrites perpendicular to the loading direction, and was pre-cycled up to 40,000 cycles on an Instron Electropuls universal test machine, using a sinusoidal waveform at 20 Hz with an applied peak load 85% yield stress (274 N) and R ratio of 0.1. Further *in situ* interrupted cyclic tests were the conducted by adding 5k, 7k, 8k, 10k, and 12k cycles sequentially to the specimen using the same loading conditions. SRCT scanning was carried out at an applied tensile load corresponding to 85% (274 N) of yield stress at each cycling interval, to hold the cracks open and to allow observations within the resolution limit of the SRCT. Scanning parameters are listed in Table 4.

Cracks were segmented from CT volumes using the seeded region growth tool in VG Studio MAX software. These were performed at 40k and 52k cycles to compare differences in crack growth and crack morphology. Carbide and void information were segmented using a global threshold approach in ImageJ software. The threshold value was determined by following an ISO50 approach [39]. The BoneJ analyse particles plugin tool for ImageJ was used to quantify the size and distribution of carbides and voids in the material. Segmented features were imported into VG Studio MAX software for 3D rendering and visualisation.

Table 4 Parameters of the SRCT scans conducted in Spring-8

Parameters	
Energy	53 keV
Voxel resolution	1.0 μm
Scan time	1.2 h
Field of view	~1.0 × 1.0 ×1.0 mm^3
Number of projections	1800
Exposure time	2 s
Dectector bining	2 × 2

3. Results

3.1 Microstructures of CM247LC alloy

Two typical dendrite morphologies were observed at the surfaces parallel and perpendicular to the solidification direction as shown in Figs. 2(a) and (b). Elongated straight columnar grains were observed on the surface parallel to the solidification direction. The width of the columnar grains is ~ 1.2 mm. Primary dendrites are parallel to the solidification direction, while secondary dendrites are perpendicular to the solidification direction, acting as connecting bridges between primary dendrites. Randomly distributed grains were observed on the surface perpendicular to the solidification direction. Primary dendrite branches were observed in this view, and it was found these branches grew in random different directions (showing the common alignment of the primary growth direction but random secondary arm orientation perpendicular to this as expected in columnar grains produced by directional solidification).

There are two types of carbides in the alloy. One is identified as blocky carbides and the other as chain-like carbides according to their morphology (Figs. 2(c) and (d)). The large blocky carbides mainly precipitated at inter-dendritic regions and partially formed at grain boundaries (GBs), while the small chain-like carbides are formed merely at GBs. Their chemical compositions were determined by SEM-EDS in Figs. 2(e) and (f). Blocky carbides are rich in Hf and the chain-like carbides are rich in W, Co, Cr. Another common phase in Ni-based superalloy, *i.e.* eutectic ($\gamma + \gamma'$), was found to precipitate at both the inter-dendritic regions and at GBs. The morphology of the secondary γ' was revealed after electro-etching. Cubic secondary γ' with a size of hundreds of nanometers and tertiary γ' with a size of several nanometers are shown in Fig. 2(g).

The visualized 3D renderings and statistical data obtained from SRCT are presented in Fig. 3. The porosity volume fraction is 0.061% in the alloy (Fig. 3(a)), which is far less than that reported for many DS and SX superalloys like MD2 and CMSX-4 [16, 23]. Most pores are smaller than 3000 μm^3 in volume and have a near spherical shape as shown in Figs. 3(b) and (c). In contrast, the volume fraction of carbides is quite high, up to 1.235% (Fig. 3(d)), and the carbide size is more varied, ranging from 1000 to over 25000 μm^3 (Fig. 3(e)). These are distributed at the inter-dendritic regions and often associated with pores as shown in Fig. 3(f), an image of the projection plane normal to the solidification direction. From the 2D observation via OM and SEM, carbides are indeed largely precipitated at the inter-dendritic regions, but pores are seldom observed in those regions due to their low volume fraction. It should be noted that the carbide precipitation along GBs cannot be reflected by the 3D renderings, because the size of the chain-like carbides is lower than the minimum resolution of SRCT and also the narrow gauge of the dog-bone specimen is smaller than the average columnar grain size, meaning that potentially no grain boundary is included in the CT scanning region.

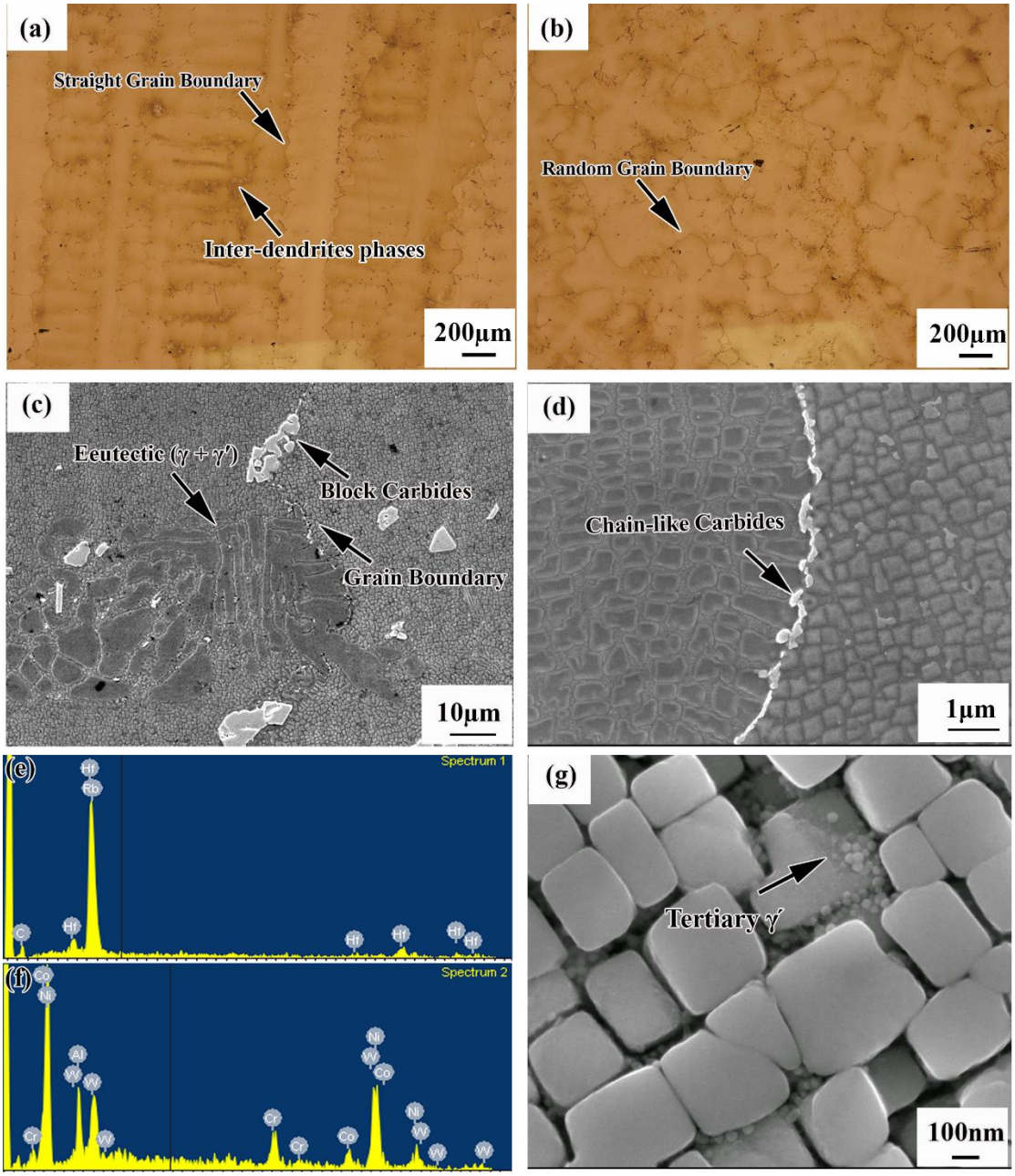

Figure 2 Microstructure of CM247LC alloy: (a) Morphology of dendrites at the surface parallel to solidification direction; (b) Morphology of dendrites at the surface perpendicular to solidification direction; (c) morphology of eutectic (γ + γ′) and blocky carbides; (d) morphology of grain boundary and chain-like carbides; (e) and (f) EDX analysis of blocky carbides and chain-like carbides; (g) secondary γ′ and tertiary γ′.

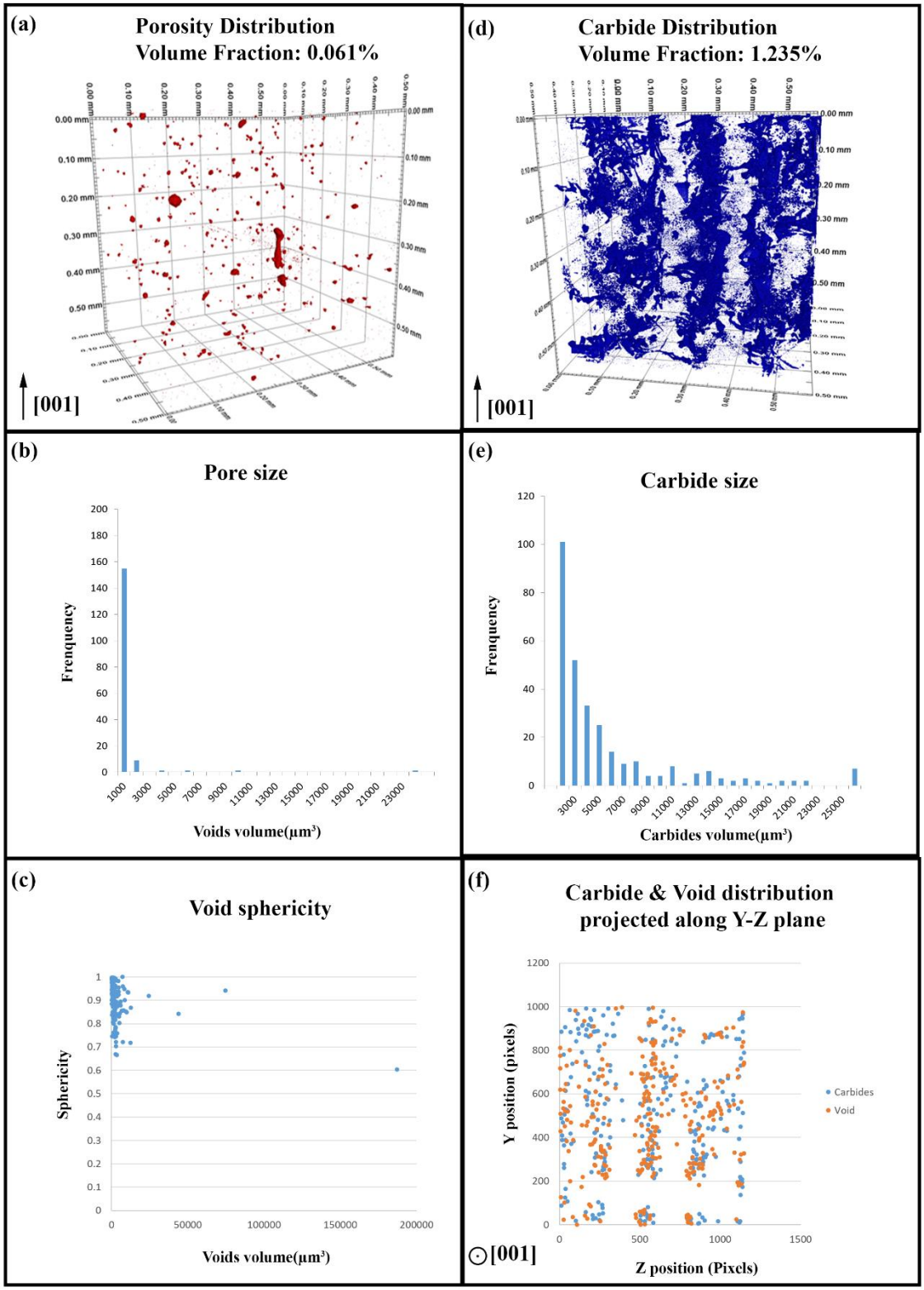

Figure 3. SRCT characterization of voids and carbides in CM247LC alloy: (a) pores distribution in 3D; (b) quantified statistical distribution of pore size; (c) pore sphericity; (d) carbide distribution in 3D; (e) quantified statistical distribution of carbide size; (f) projection of voids and carbides to a plane normal to the solidification direction of CM247LC alloy

3.2 Fatigue Crack Initiation and Early Propagation

The overall fatigue lifetime of PBB and dog-bone specimens are listed in Table 5. The apparent scatter in fatigue lifetime, is possibly attributed to the microstructure variation in the narrow gauge region. Short cracks are sensitive to microstructural features, and the local variation in size, location and shape of carbides and pores in a small gauge section could lead to quite different crack initiation behavior and finally cause a highly scattered fatigue lifetime. However, the aim of the present work is not to directly analyze the scatter in lifetime, but to assess the effects of microstructure features on fatigue crack initiation and propagation behavior.

Table 5 Summary of the fatigue test results

Specimens	Load	PPB	Dog-Bone	Dog-Bone
Test Type	———	Interrupted	Interrupted	Tested to failure
Fatigue lifetime	~ 95% yield stress	78,540	———	———
Fatigue lifetime	~ 85% yield stress	_____	135,113; 230,772	32,255; 152,611;

The morphology of the main crack is presented in Fig. 4(a), which can be divided into three regions according to the crack propagation behavior. In region 1 (R1), the main crack generally propagated inclined to the loading direction, with an angle of nearly 67.5^{o} (measured by Image J). This indicates that the main crack in this region is in stage I of the fatigue process, where cracks follow a single slip system in this 2D view. According to the replica record (Fig. 4(b)), two sub cracks were initiated from R1, and propagated in the same inclined direction to coalesce as the main crack. A deflected path occurred at the coalescence point of the two cracks and a “lump” in R1 was formed because of the deflected path. In region 2 (R2), the path of the main crack became tortuous, which might be related to the activation of multiple slip systems moving into the stage II crack growth regime. However, little information on the crack propagation behavior was recorded in this region as it was close to final fracture and the replica record was limited. In region 3 (R3), the main crack was perpendicular to the loading direction and propagated so fast that no crack history was captured by the replica record. A large plastic zone can be observed near to this region, indicating the

main crack unstably propagated to fracture. The fracture surface was reconstructed by Alicona and is shown in Fig. 4(c). The inclined and perpendicular crack paths in R1 and R3 were marked by white arrows on the fracture surface. Large amounts of slip steps were observed close to R1, whilst a dendritic fracture surface is observed close to R3 and in fracture surface regions far from R1. Crack initiation sites were identified by combining the replica record observations and associated fracture features. These initiation sites were usually at the origins of slip steps. Cracks were confirmed to initiate from carbides via SEM when observed at a higher magnification (Figs. 4(d) and (e)), and a large number of slip steps were found to emanate from the carbides which extended in different directions.

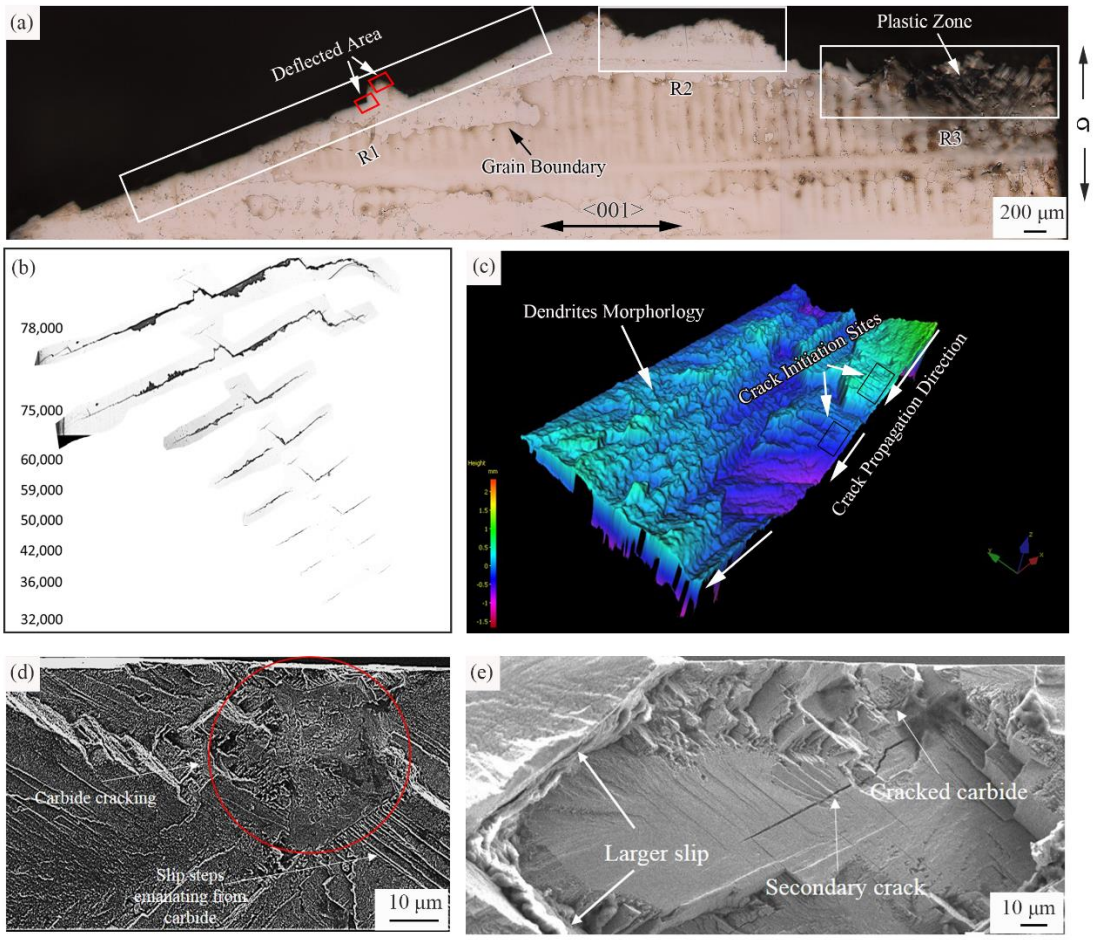

Figure 4 (a) Morphology of the main crack under OM; (b) replicas of the main crack; (c) Morphology of fracture surface; (d) and (e) initiation sites of the main crack

Secondary cracks were observed close to R1, R2 and R3 as shown in Fig. 5. A handful of micro cracks were found in R1. These secondary cracks mainly initiated at the interior or at the interface of blocky carbides in Figs. 5(a) and (b), although slip

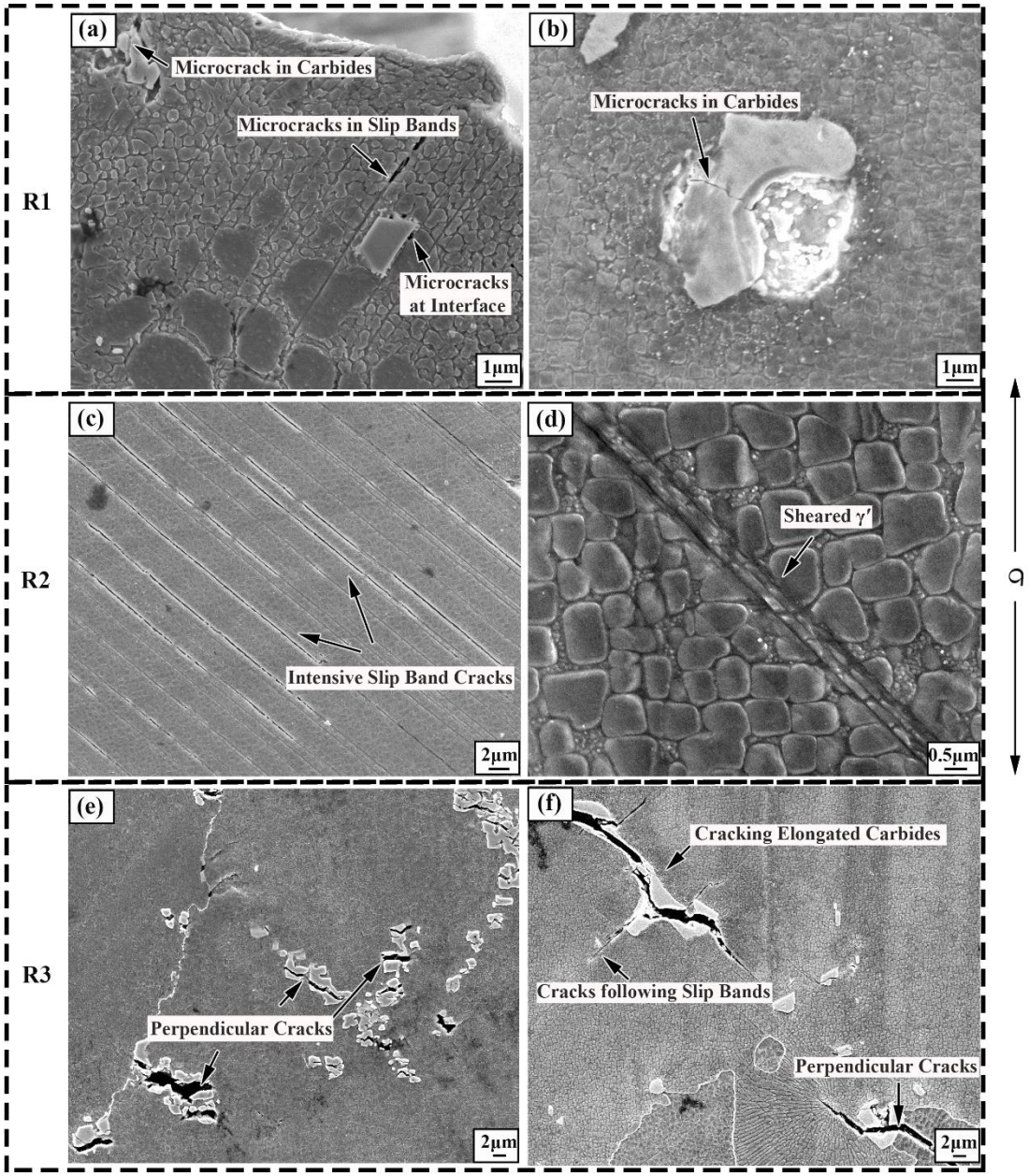

Figure 5 (a) and (b) secondary cracks in R1; (c) and (d) slip band cracking and sheared γ′ in R2; (e) and (f) carbides cracking in R3

band cracking was also observed at the "lump" of R1. To differentiate from secondary cracks in other regions, the cracks seen in R1 are designated as microstructure-induced cracking. In R2, the number of secondary cracks sharply increased, but slip band cracking became the dominant cracking mechanism (Fig. 5(c)). Secondary γ′ was severely sheared by the slip bands in this region (Fig. 5(d)), indicating the decohesion caused by dislocation motion. In R3, carbide cracking was the predominant mode of propagation of secondary cracks. However, in contrast to the cracked carbides in R1, these cracks were more likely to propagate perpendicular to the loading direction within

elongated carbides as seen in Figs. 5(e) and (f). Moreover, crack openings in these carbides are large and visible. This type of crack is designated as opening mode carbide cracks in this paper. Cracking mechanisms in R1 are not as clear as those observed in R2 and R3, and were further assessed by DIC in the following section.

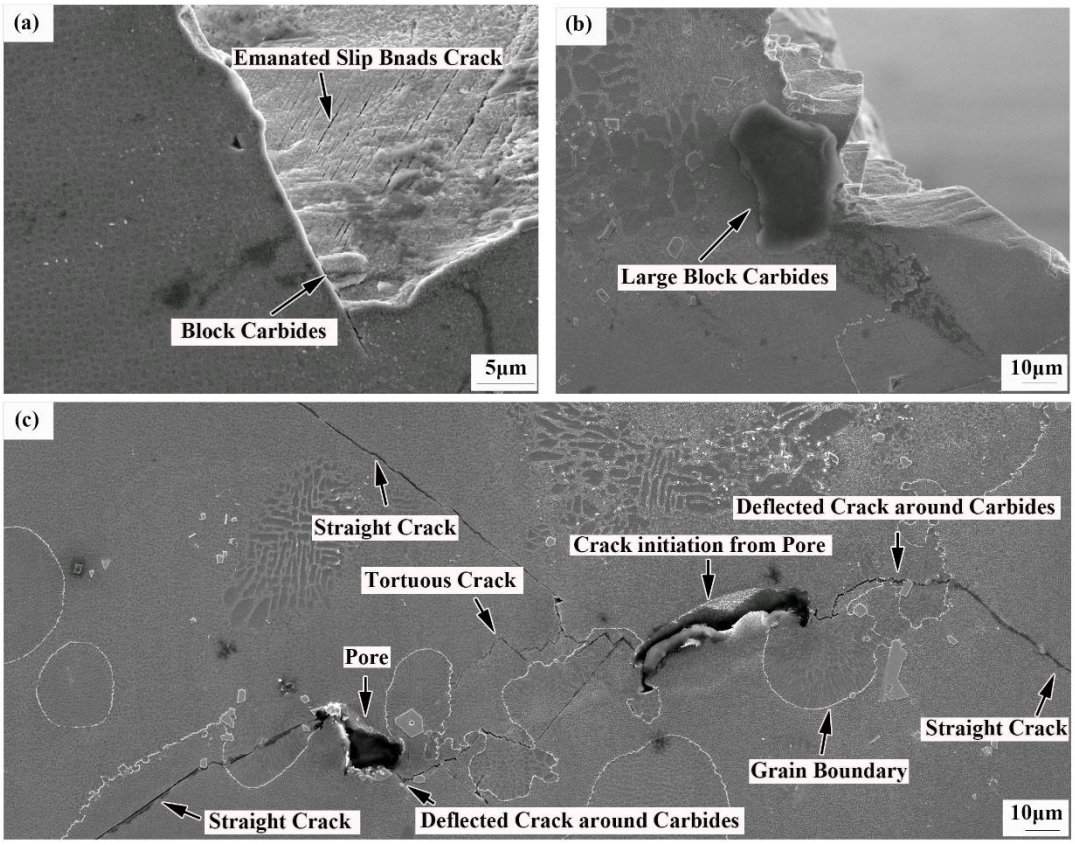

Figure 6 (a) and (b) carbides at deflected parts of main crack; (c) propagation of a secondary crack

When assessing effects of microstructure features on early crack propagation, observations were focused on the deflected areas in R1 marked by red rectangles in Fig. 4(a). This is because once the main crack has passed into stage II (e.g. in R2 and R3) the crack propagation behavior is relatively uninfluenced by microstructural features. Figs. 6(a) and (b) are SEM images of the deflected parts of the main crack. Carbides blocked crack propagation and led to a deflected or tortuous crack path as shown in the images. It is noteworthy that Fig. 6(a) showed a carbide beneath the surface which impinged on the original crack path and activated more slip systems. This means crack propagation behavior on the surface is indeed influenced by some microstructure features beneath, which is often not captured by 2D characterization. Several secondary cracks away from R1 were stitched together into Fig. 6(c). These cracks initiated from two pores at GBs, but didn't propagate along GBs, indicating that the chain-like carbides possess good resistance to cracking. After initiation from the pores, cracks

generally propagated straight (along slip-bands) within grains. However, the cracks cannot directly traverse the carbide phase, consequently the path bows or is deflected in the vicinity of carbides.

3.3 Strain localization

The early stages of strain localization were analyzed via *ex situ* SEM-DIC. The analyzed region and full-field strain distribution at 10000 cycles are presented in Fig. 7. This region contained two columnar grains, located on the left and right parts of the image, respectively, in Fig. 7(a). The grain boundary is marked in the image, though it is not very clear at this magnification. Local coordinates shown in Fig. 7(c) were chosen to express the strain components in the left grain, as the left grain takes up the majority of the full field of view. This direction was obtained from the map of maximum shear. The three in-plane strain components are shown in Figs. 7(b), (c) and (d). ε_{xx} refers to strain in the X axis direction named as longitudinal strain, ε_{yy} refers to strain in the Y axis direction named as transverse strain (*i.e.*, transverse to the maximum shear bands), and ε_{xy} is the shear strain. Strain localization of ε_{xx} was not discerned in Fig. 7 (b). In contrast, apparent transverse strain was localized within bands in the ε_{yy} map in the left grain, which is associated with crack opening or out-of-plane gliding of the slip bands, as demonstrated in [7]. Shear strain ε_{xy} was also localized within the same bands of transverse strain, and the strain is related to dislocation slip driven by pure shear stress as indicated by the sheared γ′ precipitates in Fig. 5 (d). Transverse and shear strain both traversed the whole grain, but impinged at the carbides and GB. Two AOIs were selected to be further analyzed under global coordinates using ε_{xy}^{max}, maximum shear strain as indicator. One area is in the proximity of an elongated carbide named as AOI-1, whilst the other is a carbide precipitated at a GB, named as AOI-2.

The maximum shear strain localization evolutions of AOI-1 and AOI-2 are presented in Fig. 8. Similarly straight strain bands were discerned within the grains in Fig. 8 (a), and the strain intensity was higher than 0.2 at 10000 cycles. However, *ex situ* DIC could only provide semi-quantitative assessments of strain, as significant noise was brought into the characterization by the inevitable slight changes in magnification between different images and repositioning of the specimens during the necessary series of image acquisition processes. Thus the relative strain intensity of different regions could be compared, but cannot be absolutely measured. The strain intensity increases slightly on further loading to 15000 and 22700 cycles in Figs. 8(b) and (c), and the density of strain bands is obviously increased comparing the strain maps at 10000 cycles and 22700 cycles. Some grey spots appeared within the strain bands at 227000

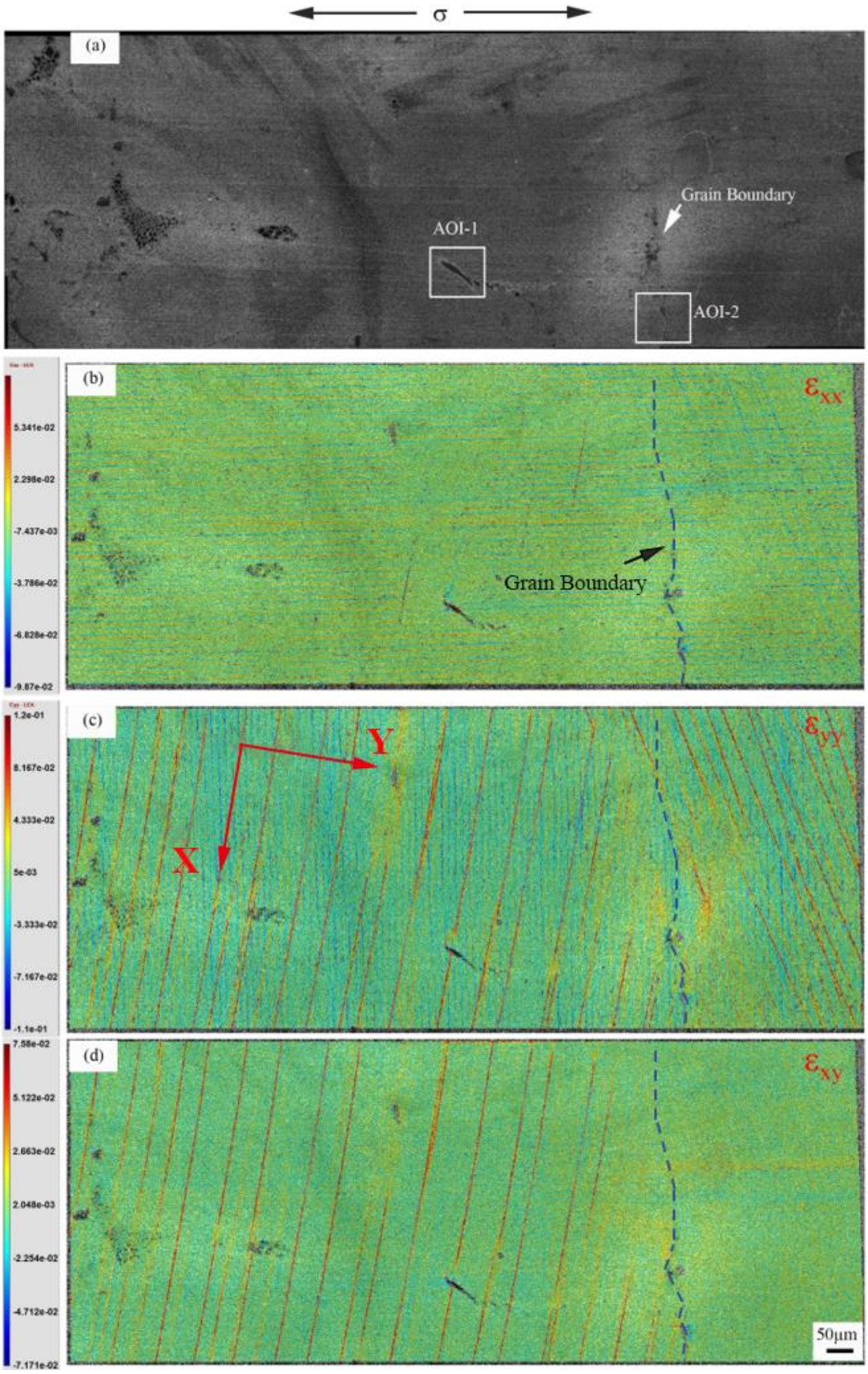

Figure 7 (a) full-field reference image; (b), (c) and (d) full-field strain maps of ε_{xx}, ε_{yy}, ε_{xy}

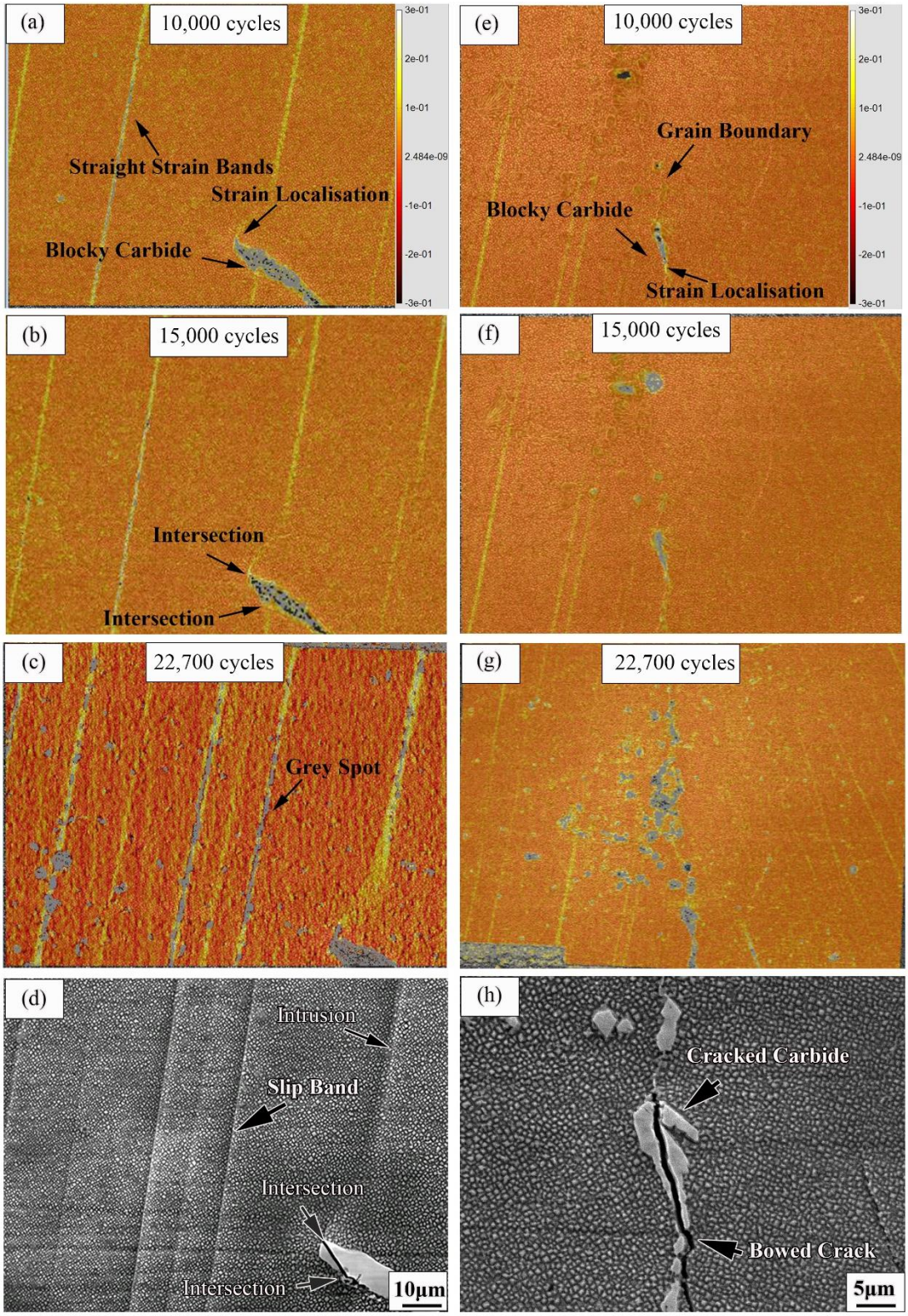

Figure 8 Maximum shear stress distribution at interior of grain (a) at 10,000 cycles; (b) at 15,000 cycles; (c) at 22,700 cycles; (d) SEM image of the carbide after 22,7000 cycles; Maximum shear stress distribution at grain boundary at (a) 10,000 cycles; (b) at 15,000 cycles; (c) at 22,700 cycles; (d) SEM image of the carbide at grain boundary after 22,7000 cycles

cycles, possibly due to the change of pattern leading to loss of correlation. Carbides are confirmed to have direct effects on material deformation, as the strain band was clearly blocked by the carbide in AOI-1 in Fig. 8(a). The intersection sites of strain bands and the carbide are indicated in Fig. 8(b), and it is interesting to observe that the crack indeed occurred at the intersection sites as shown in Fig. 8(d). Although intensive strain was localized within bands and intensive intrusion of strain bands was observed in Fig. 8(d), no cracks initiated from these bands, which indicates carbide-induced cracking occurs prior to slip band cracking. Similar carbide-induced strain localization and strain localization induced carbide cracking were reported in a polycrystalline superalloy [30]. In AOI-2, two sets of strain bands impinged on the grain boundaries in Figs. 8(e), (f) and (g). Nevertheless, the strain concentration at the proximity of the GB was not obvious until loading to 22700 cycles. In contrast, early strain localization occurred at the carbides located at the GB in Fig. 8(e), and caused the carbide cracking finally in Fig. 8(h). The crack path includes the early strain localization site marked in Fig. 8(e). It is noteworthy that the crack became bowed as it encountered the blocky carbide below in Fig. 8(h), which is consistent with the aforementioned observation of secondary crack propagation.

3.4 *In situ* SRCT Characterization

Two cracks that initiated from pores were selected for CT scanning, one of which was located at the upper parts of the 3D rendering in Fig. 9 (b), hereby referred to as upper crack (UC), and the lower one was referred to as LC. From the bottom view of the 3D rendering, the two cracks were located at a nearby side surface. The UC primary growth direction was aligned with the interdendritic regions, whilst the LC primary direction lay perpendicular to them. In Figs. 9(d), (e), (g) and (h), blue identifies pores, grey identifies carbides, red regions show the crack morphology at 40000 cycles, while the green area shows the crack morphology at 52000 cycles. Carbide distribution in the proximity of LC and UC is presented in Figs. 9(d) and (g) respectively. It is apparent the density of carbides in the vicinity of UC was much higher than that of LC, with the upper crack being within the inter-dendritic region. Crack morphology segmented by a seeded region growth algorithm was superimposed on the carbide distribution in Figs. 9(e) and (h). In the LC, nearby carbides were mainly congregated at one side of the 3D rendering, and cracking planes clearly interacted with these carbides. One cracking plane was parallel and even adjacent to a faceted carbide marked in Figs. 9(d) and (e). However, carbides at the farside seemed to have little effect on crack growth from the 3D observation. In the UC, these interactions between carbides and cracks were more obvious, as more cracking planes were induced by the surrounding carbides.

One cracking carbide was found in Fig. 9(g), and the corresponding cracking plane was marked in Fig. 9(h). This is the first report observing a cracking carbide and its associated cracking plane in 3D in a DS system, owing to the high resolution provided by SRCT. The surface slice of the two cracks were shown in Figs. 9(f) and (i). Carbides were indeed seen to be congregated at one side of the pore for the LC, which is consistent with the SRCT result. Nonetheless, only one crack was observed on the surface slice, which indicates the inadequacy of 2D observations in accurately characterizing complex crack initiation and growth behavior. Similar observations were reported in the literature [40] using destructive techniques (FIB-cross section) on several cracked carbides. The effect of sub-surface clustering of carbides and or nitrides was found to favor crack propagation and that only surface/2D observation are not sufficient to answer the problem of short crack propagation on "defect"-containing materials. More complicated cracks were observed on the surface slice of the UC, especially, one cracking carbide was captured.

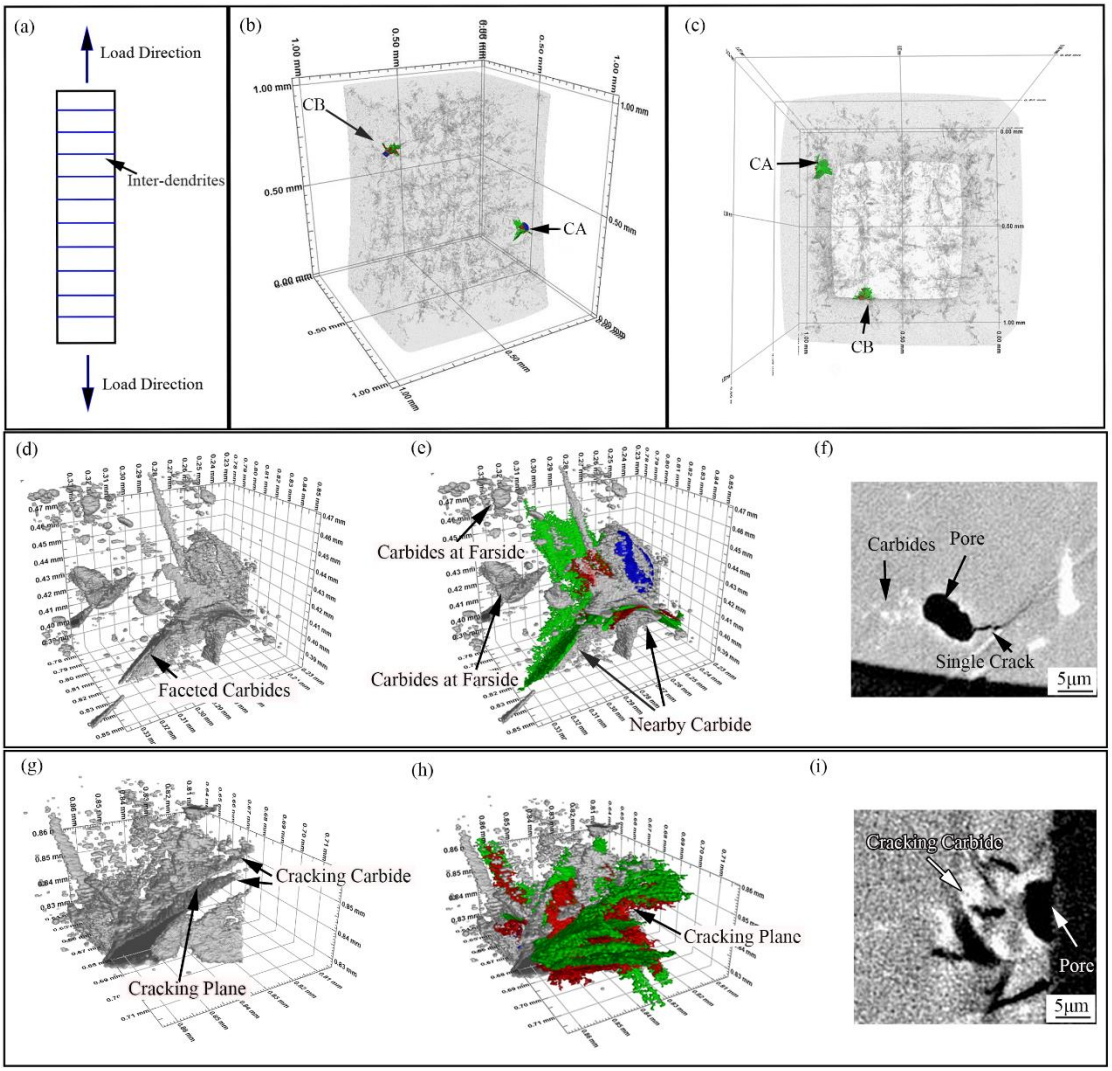

Figure 9 (a) schematic diagram of loading tension-tension test; (b) 3D rendering of the specimen in front view; (c) 3D rendering of the specimen in bottom; (d) carbides distribution around LC; (e) superimposed image of carbides and cracking planes around LC; (f) surface slice of LC; (g) carbides distribution around UC; (h) superimposed image of carbides and cracking planes around UC; (i) surface slice of UC

The evolution history of LC and UC are presented in Fig. 10, respectively. In LC, four sub cracks are named as LC1, LC2, LC3 and LC4 (Fig. 10(a)). LC1 was initiated from the pore and corresponded to the single crack observed at the surface in Fig. 9(f),

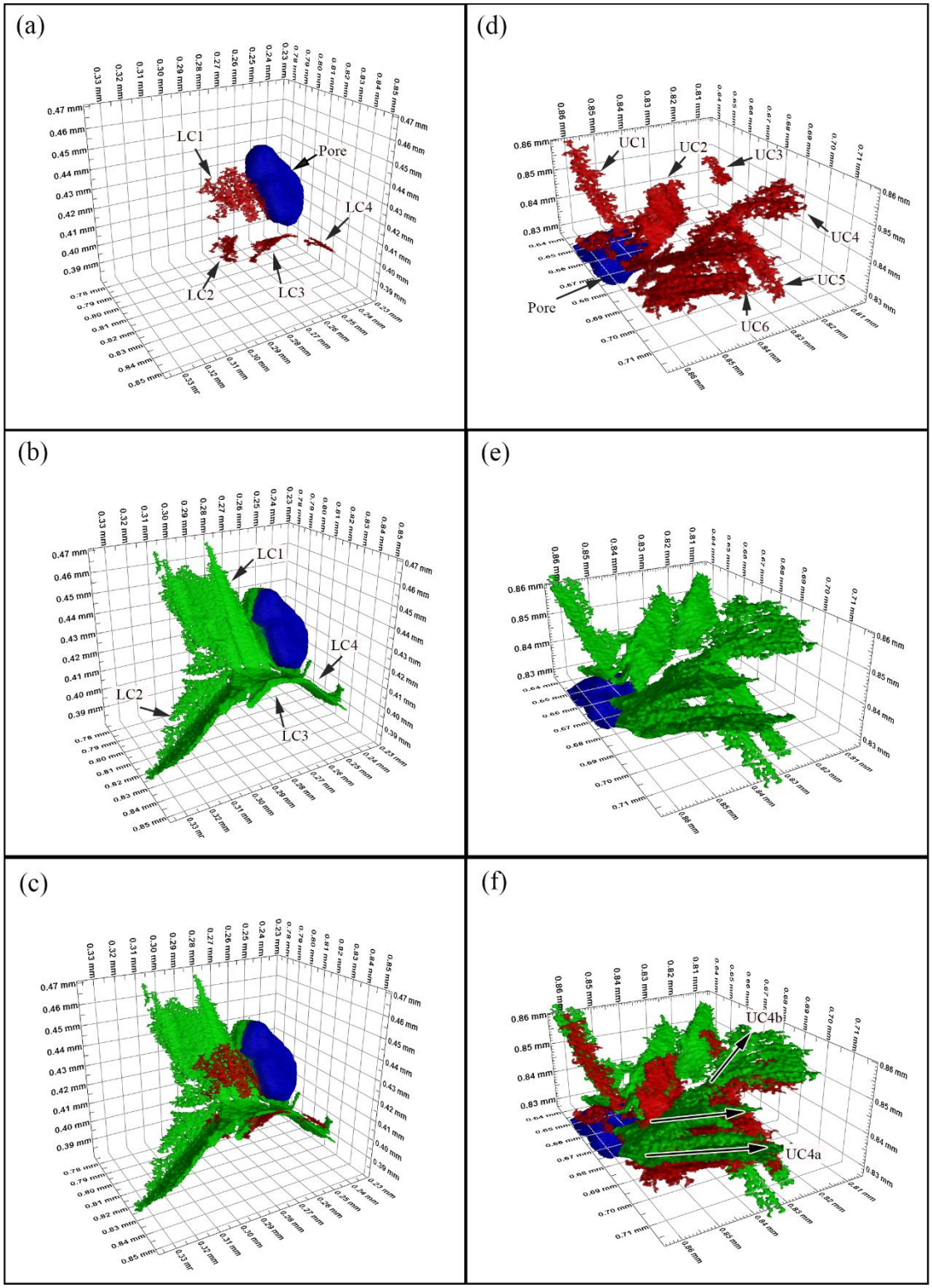

Figure 10 CT images of CM247LC crack propagation. (a) cracking planes at 40000 cycles of LC; (b) cracking planes at 52000 cycles of LC; (c) superimposed image of cracking planes at 40000 and 52000 cycles of LC; (d) cracking planes at 40000 cycles of UC; (e) cracking planes at 52000 cycles of UC; (f) superimposed image of cracking planes at 40000 and 52000 cycles of UC

whilst other cracking planes LC2, LC3 and LC4 were initiated in the bulk. The four cracking planes propagated in different directions shown in Fig. 10(b) at 52000 cycles. LC1 seems to propagate along a slip system, as nearly no carbides were present in the vicinity of the cracking plane (Fig. 9(e)), while LC2 propagated parallel to a carbide facet shown in Fig. 9(d) and Fig. 10(b). The two cracks both grew substantially as shown in Fig. 10(c). LC3 and LC4 had a very limited growth compared to LC1 and LC2, potentially because carbides were concentrated at regions that blocked LC3 and LC4 propagation. This result confirms the potential of shielding effects of carbides on crack propagation. More sub-cracks were generated in UC, named as UC1 to UC6 respectively in Fig. 10(d). Observation was focused on UC4, which was initiated from a carbide as noted above. It was found that UC5 and UC6, the two parallel cracking planes, were branches of UC4, indicating that more slip planes were activated after UC4 initiated from the carbide and propagated subsequently. On further loading to 52000 cycles in Figs. 10(e) and (f), UC4 was found to have formed by slipping mainly in two directions. One was along a carbide elongated direction, named as UC4a. The other slip direction was inclined to UC4a, named as UC4b, marked in Fig. 10(e). Thus, influenced by carbides, several cracking planes and extension directions were simultaneously activated, explaining the highly deflected crack path at the vicinity of carbides observed in the SEM.

4. Discussion

4.1 Mechanism of Secondary Crack Initiation

Three secondary cracking modes were captured in different regions in the alloy CM247LC during the fatigue process shown in Fig. 5, and they were designated as microstructure-induced cracking at early stage (R1), slip band cracking at intermediate stage (R2) and opening mode carbide cracking at the final stage (R3) respectively in this work. These cracking behaviors are normally observed in fatigue and tensile failure in these materials systems, but it is interesting to discern that most of the secondary cracks belonged to only one or two of these modes as reported in other investigations [10, 11, 13-16]. Very limited research reports these three modes of cracks operating simultaneously in one alloy to the best of our knowledge, indicating the complicated cracking mechanisms during fatigue in this DS alloy system. Texier et al. [40] presented some interesting similarities with our work but on a polycrystalline superalloy and for different loading conditions.

Microstructure-induced cracking refers to cracks induced by the interaction between dislocation movement and micro-features like defects, secondary phases and

GBs. Plastic deformation of metallic materials is linked to activation of slip systems for dislocation motion and formation of slip bands. But the plastic incompatibility between matrix and secondary phases/defects or neighboring grains prevents dislocation motion, causing strain/stress localization at the microstructural scale, thereby leading to crack initiation [7, 23, 41, 42]. Obviously carbide-induced cracking was observed in the early stages of fatigue in the current work. Strain distribution around carbides was captured via DIC in Figs. 7(b), (c) and 8(a), (b), (c). The strain was localized at the intersection of the strain bands and carbides, and then a micro crack was formed by bridging the strain accumulated sites as indicated in Fig. 8(d). Similar results were presented in another fatigue investigation on alloy CM247LC, which revealed dislocation pile-ups and tangling around carbides [26]. Moreover, this work proposed a similar explanation for carbide induced cracking, *i.e.* the cracking was caused by bridging between closely strain-located crack initiation sites. However, their experiments could not directly verify this hypothesis, which has now been directly confirmed in this study via the SEM-DIC approach. Pore-induced cracking was also observed, but it did not account for the majority of secondary cracks in R1 of the alloy due to the low volume fraction, small size and spherical shape of pores. Consistent with Jiang's elastic-plastic finite element modeling results [23], these large-sized pores with irregular shapes more easily induce strain/stress concentration at their local 'ridges'. GB-induced cracking was not observed in these tests on CM247LC. Although some cracks were initiated from pores on GBs, they propagated into the grains rather than along GBs in Fig. 6(c) and Fig. 8(h), showing the high resistance of the GB to cracking under these test conditions. Strain accumulation close to GBs was not as intensive as strain bands formed within grains, furthermore confirming that slip band-GB impingements were not preferable sites for crack initiation. Similar phenomena are also shown in studies conducted by Stinville *et.al* and Wael *et. al* [21, 27]. They showed that a dislocation could fully transmit (*i.e.* cross slip) or partially transmit through GBs, particularly in the case of grains with low angle GBs and small tilt angle of slip planes in adjacent grains. In addition, small-scale precipitates on GBs enhance the cracking resistance in Chen's investigation [43], and the enhanced cracking resistance is attributed to the small scale (even nano-scale) of GB phases. Because the nano-scale phases not only strengthen the GBs, but also are able to pin dislocations at GBs, hindering GB slip or migration during plastic deformation. Thus, the high cracking resistance of GBs observed in this study is probably attributed to two factors, one of which is the release of strain accumulation related to dislocation transmission, and the other is the nano-scale carbides precipitated on the GB shown in Fig. 3(d).

Slip band cracking was the dominant source of secondary cracks in R2. The micro cracks initiated within slip bands and coalesced to form straight cracks in Fig. 5(c). The cracking mechanism is associated with γ′ decohesion in slip bands, caused by repeated dislocation shearing. During fatigue tests, dislocations are forced to move back and forth within the slip bands, shearing γ′ and causing severe decohesion and potential dissolution along the slip band . Micro voids hence nucleate and grow in the slip bands to form micro cracks [44]. According to Pang's work, slip band cracking is mostly generated in alloys with a large grain size, which can facilitate the formation of long planar slip lengths [15]. Another feature of slip band cracking is reported in Jiang's investigation, where severely sheared γ′ precipitates within slip bands could be a clear indicator for slip band cracking [7, 23]. Consistent with the aforementioned research, the large columnar grains of CM247LC are prone to slip band cracking, whilst extensive shearing of the γ′ precipitates is also observed (Fig. 5(d)). Moreover, slip band cracking lagged behind carbide induced cracking which was characterized by DIC in this work. Strain intensity within slip bands and at intersection of carbides were both over 0.2 (a very high apparent strain intensity) at 22700 cycles in Fig. 8(c) and (h). However, cracks were initiated at carbides. Slip bands at the sides of cracking carbides still remained uncracked (no obvious slip band cracking is observed) in Figs. 8(d) and (h). The result is in agreement with the three-point bending test. Carbide induced cracking mainly occurred at R1, the early stage, while slip band cracking occurred at R2, the intermediate stage. This delay in slip band cracking, compared to carbide induced cracking, has not been reported and explained previously. It seems then that the formation of long planar slip bands and decohesion of γ′ might require more cycling than dislocation pile-ups at carbides, with the latter providing a more potent initiation mechanism.

Opening mode carbide-cracking occurred at the last stage of fatigue (R3), where cracks inside of carbides propagated nearly perpendicular to the loading direction with a large apparent crack opening displacement. In fact, this phenomenon is often observed in tension tests, where materials experience substantive plastic deformation, not only in fatigue failure (where small scale and progressive cyclic plastic deformation processes build up more gradually and sparsely throughout the material). Lindley *et.al* [45] proposed that dislocation pile-up mechanisms were unable to explain the result, as dislocation pile-up sites at carbides would be random, so there should be equal possibilities to crack carbides at all angles to any loading direction. Fiber loading mechanisms might be a more appropriate explanation [46]. This assumes that the matrix does not slip only along one specific direction when the macro stress reaches quite a

high level, above yield stress. General shear stress exerted on the phase surface by the plastically yielding matrix is balanced by internal tensile stresses in the secondary phase. Thus, the total internal stress of the secondary phase is related to the macro plastic strain of the matrix. As a result, perpendicular cracks within the brittle carbides would preferentially occur (the carbides are directly loaded overall and crack, rather than the local impingement of a slip band causing only a very localized stress on the carbide) [47].

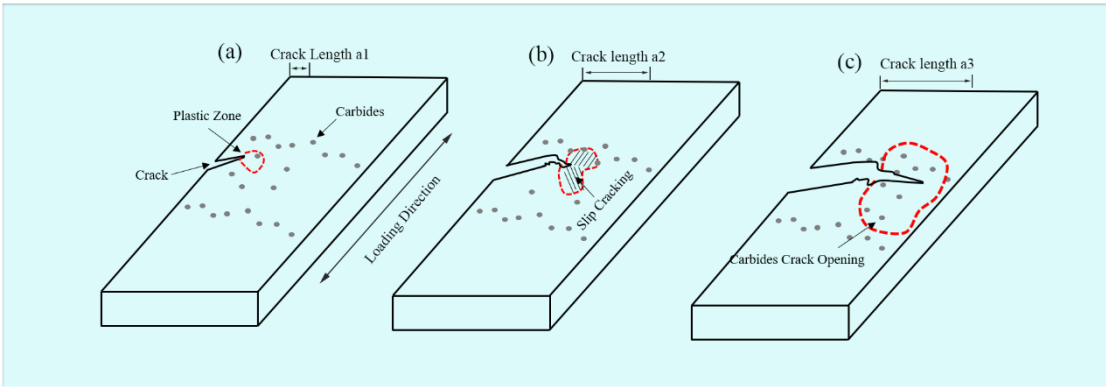

Fig. 11 (a) schematic diagram of main crack at the early stage; (b) at the medium stage; (c) at the last stage

The different cracking behaviors in CM247LC can be inferred to be associated with the growing plastic region at the main crack tip shown in a schematic diagram in Fig. 11, based on the cracking mechanism discussed above and crack evolution history. At the early stage of the fatigue process, the main crack was in stage I, propagating along one slip direction inclined to the loading direction, shown in Fig. 11(a). The plastic zone of the crack tip is related to crack length according to Von-Mises yield criterion. In R1 (Fig 11(a)), the area of plastic zone is the smallest compared to that formed in R2 and R3, and is non conducive for the formation of long planar slip bands. In this stage, carbide-induced cracking is the dominant crack initiation behavior in the region. However, only a handful of carbides are included in such a small plastic zone, so the number of cracks observed in R1 are much less than in R2 and R3. With the increase in crack length, the plastic zone extended as shown in Fig. 11(b). Meanwhile, the main crack transitioned into stage II of the fatigue process, where multiple slip systems were activated, and thereby the main crack path became tortuous. The enlarged plastic zone facilitated the formation of planar slip, giving rise to (observed) slip band cracking. In this stage, both slip band cracking and carbide induced cracking could notionally occur, but from the observation of R2 in Fig. 4 (c), slip band cracking became the predominant crack initiation behavior. This was thought to be caused by two factors. Firstly, the plastic zone of the crack tip was believed to not be large enough to extend

into the inter-dendritic region nearby, where carbides were congregated, as shown in Fig. 1(a) and Fig. 11(b). The second reason is that the heterogeneous plastic strain was concentrated within slip bands, as shown in Fig. 8. Carbides contained in the plastic zone could be located between these strain bands, therefore, strain accumulation around these carbides was insignificant. As a result, less carbide induced cracking was observed than slip band cracking in R2. When the main crack propagated from R2 to R3, it became perpendicular to loading direction. The plastic zone at the crack tip became much larger, causing relatively fast fatigue fracture. The inter-dendritic region was then partially covered by the extended plastic zone, and lots of carbides exhibiting brittle cracking were observed in Figs. 4(e) and (f). As discussed above, the increased macro plastic strain gave a rise to the higher internal tension stress within the carbides, and caused them to crack perpendicular to the loading direction (opening mode carbide cracking occurred).

4.2 Comparison of Crack growth behavior in 2D and 3D

The 3D morphology of early cracking planes and surrounding carbides are presented and described in detail in Figs. 9 and 10. To the best of our knowledge, this is the first time in characterizing the interaction between cracks and carbides at a submicron scale in 3D, owing to the high resolution of SRCT and appropriate segmentation strategies [32]. Effects of carbides on inducing cracking and shielding crack propagation were both captured in 3D renderings, as firstly, more cracks were observed initiated at the region with a high density of carbides in Fig. 9. When the cracking plane extension appeared to be blocked, another propagation direction was activated by the congregated carbides, see Fig. 10. The results are mostly consistent with the 2D observation, in which cracks were found initiated at strain localisation sites of blocky carbides (Fig. 8). Otherwise straight crack paths were deflected and tortuous at the proximity of carbides, see Fig. 6. However, the chain-like carbides at grains boundaries could not be captured in SRCT, as these carbides are of the order of ~100s nm, lower than the minimum resolution of SRCT. Also, the narrow field of view and low penetration for nickel base superalloy is another factor limiting characterizing the chain-like carbides, as reported in Marine's research [28].

The crack propagation behaviour within grains in the DS superalloy CM247LC is compared with that in polycrystal and single crystal alloys in Fig. 12. In the polycrystal alloy, faceted cracks mainly grow on the most favourable plane within grains. These activated crack planes are influenced by the co-effects of resolved shear stress (Schmid factors) and neighbouring grains [7, 33, 48]. Two neighbouring grains of polycrystal alloys are shown in Fig. 12(a) extracted from Hassanipour's research [41], named as

grain 149 and 160. In grain 149, three slip planes of high shear stress (Schmid factors) might be activated. However, to minimize the mismatch angle of cracking plane in 160, one slip plane is activated eventually [41]. These phenomena have been found in many previous studies on crack growth behaviour in polycrystal alloys [7, 21, 37, 48]. Some of the research is however based on 2D observation, in which it is assumed that the straight crack observed at the surface within grains corresponds to a facet-like crack growing along one slip plane. The selection of crack path is determined by both activated slip systems and crack geometry compatibility when the crack propagates into the neighbouring grains in poly crystalline superalloy. In the DS alloy CM247LC, four facet-like cracks were activated within an individual grain (Fig. 12 (b)), although only one straight crack was observed at the surface (Fig. 9(f)). This crack behaviour is more closely to linked to that in the single crystal alloy in Fig. 12(c), where two slip planes were activated from a pore [23]. It is reasonable to infer that the simultaneous activation of several cracking planes is attributed to the minimized effects of neighboring grains. Firstly, in the DS alloys CM247LC, the columnar grains possess fewer surrounding grains, because there are no neighboring grains along their longitudinal direction. Secondly, the intragranular area is larger than most of polycrystal alloys, as the average width of the columnar grains reached 1.2 mm. In addition, columnar grains have a more uniform elongated direction which is conducive to compatible deformation compared to polycrystal alloys. Therefore, the deformation of intragranular areas is less constrained by neighboring grains, and more slip systems for crack growth could be activated. However, more characterization work still needs to be done to further verify this hypothesis.

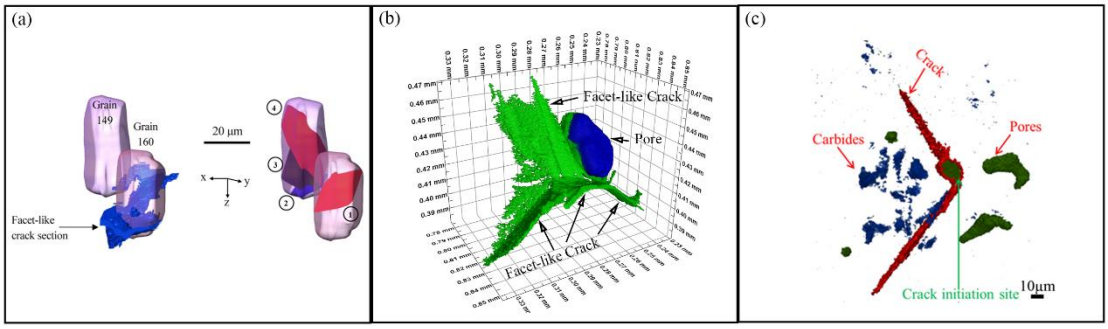

Figure 12 (a) Facet-like crack section in polycrystal alloys [41]; (b) facet-like crack sections in DS alloys CM247LC; (c) 3D crack morphology in single crystal ally [23].

5. Conclusions

(1) SRCT can accurately capture the location, size and morphology of blocky carbides and pores in CM247LC alloy. It is found the two microstructural features are mainly congregated in the inter-dendritic region. Chain-like carbides at grain boundaries

cannot be characterized in the technique because their size is lower than the SRCT resolution employed here.

(2) Three modes of secondary crack behaviors are identified in the proximity of the main crack. In the early stages of the fatigue process, a few carbides become the main sites inducing secondary crack formation. As the length of main crack increases, more extended slip band cracking forms. In the final stage, the fiber loading damage of carbides occurs.

(3) The effects of carbides on inducing crack formation and shielding crack propagation are identified by the *in situ* 3D observation of cracking planes. Also, it is found several cracking planes are formed simultaneously at the proximity of pores from the 3D analysis, indicating that cracks grow on several slip planes around such stress concentration features rather than along just one favorable slip plane in the early stage of fatigue.

Acknowledgement

The authors would like to thank the EPSRC (Grant no: EP/M000710/1) for funding support and the China Scholarship Council, China, for financial support. Dr. R. Jiang would like to thank the National Natural Science Foundation of China [Grant no: 51805251] for financial support. S. Octaviani gratefully acknowledges support from Schlumberger Faculty for the Future Programme and the Roberto Rocca Education Programme. The synchrotron radiation experiments were performed at the BL20XU beamline in SPring-8 with the approval of the Japan Synchrotron Radiation Research Institute (JASRI) (Proposal number 2016A1278). The authors are grateful for the travel funding provided by the Great Britain Sasakawa Foundation and the Global Partnership Award from University of Southampton to visit Spring-8. The authors also would like to thank the MatchID team for provision of the MatchID software. The authors also would like to acknowledge Prof. Liguo Zhao at Loughborough University, Dr. Mark Hardy at Rolls-Royce, Dr. Matthew Lunt at Defence Science and Technology Laboratory, Dr. Gordon McColvin at GE Power, Prof Michael Preuss and Dr. João Quinta da Fonseca at University of Manchester and Prof. Scott Lockyer at Uniper Technologies Ltd for several useful discussions and comments of the results presented in this paper.

Dataset statement

Supporting data is available from the University of Southampton Institutional repository on request from http://dx.doi.org/10.5258/SOTON/D1651

References

[1] G.L. Erickson, K. Harris, R.E. Schwer, Directionally Solidified DS CM 247 LC—Optimized Mechanical Properties Resulting From Extensive γ′ Solutioning, ASME 1985 International Gas Turbine Conference and Exhibit, 1985.

[2] J.M. Martinez-Esnaola, A. Martin-Meizoso, E.E. Affeldt, A. Bennett, M. Fuentes, High temperature fatigue in single crystal superalloys, Fatigue & Fracture of Engineering Materials & Structures 20(5) (1997) 771-88.

[3] A. Pineau, S.D. Antolovich, High temperature fatigue of nickel-base superalloys – A review with special emphasis on deformation modes and oxidation, Engineering Failure Analysis 16(8) (2009) 2668-2697.

[4] V. Lupinc, G. Onofrio, The effect of creep and oxidation on high-temperature fatigue crack propagation in 〈001〉-loaded CMSX-2 superalloy single crystals, Materials Science and Engineering: A 202(1) (1995) 76-83.

[5] Z. Mei, C.R. Krenn, J.W. Morris, Initiation and growth of small fatigue cracks in a Ni-base superalloy, Metallurgical and Materials Transactions A 26(8) (1995) 2063-2073.

[6] R.R. Stephens, L. Grabowski, D.W. Hoeppner, The effect of temperature on the behaviour of short fatigue cracks in Waspaloy using an in situ SEM fatigue apparatus, International Journal of Fatigue 15(4) (1993) 273-282.

[7] R. Jiang, F. Pierron, S. Octaviani, P.A.S. Reed, Characterisation of strain localisation processes during fatigue crack initiation and early crack propagation by SEM-DIC in an advanced disc alloy, Materials Science and Engineering: A 699 (2017) 128-144.

[8] M. Boeff, H. Hassan, A. Hartmaier, On the numerical modeling of nucleation and growth of microstructurally short cracks in polycrystals under cyclic loading, Journal of Materials Research 34 (2019) 1-12.

[9] Q.-S. Chen, P. Zhu, M. He, Simulations of dislocation density in silicon carbide crystals grown by the PVT-method, Journal of Crystal Growth 531 (2020) 125380.

[10] J. Gayda, R.V. Miner, The effect of microstructure on 650 °C fatigue crack growth in P/M astroloy, Metallurgical Transactions A 14(11) (1983) 2301.

[11] Q. Han, Y. Gu, S. Soe, F. Lacan, R. Setchi, Effect of hot cracking on the mechanical properties of Hastelloy X superalloy fabricated by laser powder bed fusion additive manufacturing, Optics & Laser Technology 124 (2020) 105984.

[12] Y. Jiao, Y. Zhang, S. Ma, D. Sang, Y. Zhang, J. Zhao, Y. Liu, S. Yang, Role of secondary phase particles in fatigue behavior of high-speed railway gearbox material, International Journal of Fatigue 131 (2020) 105336.

[13] Z. Liao, B. Yang, Y. Qin, S. Xiao, G. Yang, T. Zhu, N. Gao, Short fatigue crack behaviour of LZ50 railway axle steel under multi-axial loading in low-cycle fatigue, International Journal of Fatigue 132 (2020) 105366.

[14] X. Meng, D. Zhang, Z. Weiwen, Q. Cheng, G. Liang, J. Chen, Microstructure and mechanical properties of a high-Zn aluminum alloy prepared by melt spinning and extrusion, Journal of Alloys and Compounds 819 (2020) 152990.

[15] H.T. Pang, P.A.S. Reed, Effects of microstructure on room temperature fatigue crack initiation and short crack propagation in Udimet 720Li Ni-base superalloy, International Journal of Fatigue 30(10) (2008) 2009-2020.

[16] B. Ruttert, C. Meid, L. Mujica Roncery, I. Lopez-Galilea, M. Bartsch, W. Theisen, Effect of porosity and eutectics on the high-temperature low-cycle fatigue performance of a nickel-base single-crystal superalloy, Scripta Materialia 155 (2018) 139-143.
[17] Y. Liu, M. Kang, Y. Wu, M. Wang, M. Li, J. Yu, H. Gao, J. Wang, Crack formation and microstructure-sensitive propagation in low cycle fatigue of a polycrystalline nickel-based superalloy with different heat treatments, International Journal of Fatigue 108 (2018) 79-89.
[18] P. Peralta, C. Laird, Compatibility stresses in fatigued bicrystals: Dependence on misorientation and small plastic deformations, Acta Materialia 45(12) (1997) 5129-5143.
[19] T. Denda, P.L. Bretz, J.K. Tien, INCLUSION SIZE EFFECT ON THE FATIGUE CRACK-PROPAGATION MECHANISM AND FRACTURE-MECHANICS OF A SUPERALLOY, Metallurgical Transactions a-Physical Metallurgy and Materials Science 23(2) (1992) 519-526.
[20] D. Texier, A.C. Gomez, S. Pierret, J.-M. Franchet, T.M. Pollock, P. Villechaise, J. Cormier, Microstructural Features Controlling the Variability in Low-Cycle Fatigue Properties of Alloy Inconel 718DA at Intermediate Temperature, Metallurgical and Materials Transactions A: Physical Metallurgy and Materials Science 47(3) (2016) 1096-1109.
[21] J.C. Stinville, N. Vanderesse, F. Bridier, P. Bocher, T.M. Pollock, High resolution mapping of strain localization near twin boundaries in a nickel-based superalloy, Acta Materialia 98 (2015) 29-42.
[22] L. Wang, N. Limodin, A. El Bartali, J.-F. Witz, R. Seghir, J.-Y. Buffiere, E. Charkaluk, Influence of pores on crack initiation in monotonic tensile and cyclic loadings in lost foam casting A319 alloy by using 3D in-situ analysis, Materials Science and Engineering: A 673 (2016) 362-372.
[23] R. Jiang, D.J. Bull, A. Evangelou, A. Harte, F. Pierron, I. Sinclair, M. Preuss, X.T. Hu, P.A.S. Reed, Strain accumulation and fatigue crack initiation at pores and carbides in a SX superalloy at room temperature, International Journal of Fatigue 114 (2018) 22-33.
[24] K. Harris, G. Erickson, R. Schwer, MAR M 247 derivations—CM 247 LC DS alloy, CMSX® single crystal alloys, properties and performance, 5th Int. Symp, 1984, pp. 221-230.
[25] Z. Moore, R. Neu, Creep fatigue of a directionally solidified Ni‐base superalloy–smooth and cylindrically notched specimens, Fatigue & Fracture of Engineering Materials & Structures 34(1) (2011) 17-31.
[26] K. Prasad, R. Sarkar, K. Gopinath, Role of shrinkage pores, carbides on cyclic deformation behaviour of conventionally cast nickel base superalloy CM247LC® at 870°C, Materials Science and Engineering: A 654 (2016) 381-389.
[27] W.Z. Abuzaid, M.D. Sangid, J.D. Carroll, H. Sehitoglu, J. Lambros, Slip transfer and plastic strain accumulation across grain boundaries in Hastelloy X, Journal of the Mechanics and Physics of Solids 60(6) (2012) 1201-1220.
[28] F. Di Gioacchino, J. Quinta da Fonseca, Plastic Strain Mapping with Sub-micron Resolution Using Digital Image Correlation, Experimental Mechanics 53(5) (2013) 743-754.
[29] A.L. Hijazi, A Novel Approach for the Determination of Surface Tilt Angles in Two-Dimensional Digital Image Correlation Experiments, Experimental Mechanics 60(3) (2020) 267-282.
[30] D. Texier, J.-C. Stinville, M.-A. Charpagne, Z. Chen, V. Valle, P. Villechaise, T.M. Pollock, J. Cormier, Role of Non-metallic Inclusions and Twins on the Variability in Fatigue Life in Alloy 718 Nickel Base Superalloy, 14th International Symposium on Superalloys, Superalloys 2021, September 12, 2021 - September 16, 2021, Springer Science and Business Media Deutschland GmbH, Seven Springs, PA, United states, 2020, pp. 629-639.

[31] T.F. Morgeneyer, L. Helfen, I. Sinclair, H. Proudhon, F. Xu, T. Baumbach, Ductile crack initiation and propagation assessed via in situ synchrotron radiation-computed laminography, Scripta Materialia 65(11) (2011) 1010-1013.
[32] E. Maire, P.J. Withers, Quantitative X-ray tomography, International Materials Reviews 59(1) (2014) 1-43.
[33] R. Jiang, N. Karpasitis, N. Gao, P.A.S. Reed, Effects of microstructures on fatigue crack initiation and short crack propagation at room temperature in an advanced disc superalloy, Materials Science and Engineering: A 641 (2015) 148-159.
[34] C. Altenbach, C. Schnatterer, U.A. Mercado, J.-P. Suuronen, D. Zander, G. Requena, Synchrotron-based holotomography and X-ray fluorescence study on the stress corrosion cracking behavior of the peak-aged 7075 aluminum alloy, Journal of Alloys and Compounds 817 (2020) 152722.
[35] D.J. Bull, S.M. Spearing, I. Sinclair, L. Helfen, Three-dimensional assessment of low velocity impact damage in particle toughened composite laminates using micro-focus X-ray computed tomography and synchrotron radiation laminography, Composites Part A: Applied Science and Manufacturing 52 (2013) 62-69.
[36] R. Jiang, D.J. Bull, D. Proprentner, B. Shollock, P.A.S. Reed, Effects of oxygen-related damage on dwell-fatigue crack propagation in a P/M Ni-based superalloy: From 2D to 3D assessment, International Journal of Fatigue 99 (2017) 175-186.
[37] M. Hassanipour, S. Watanabe, K. Hirayama, H. Li, H. Toda, K. Uesugi, A. Takeuchi, Assessment of predominant microstructural features controlling 3D short crack growth behavior via a surrogate approach in Ti-6Al-4V, Materials Science and Engineering: A 751 (2019) 351-362.
[38] H.W. Schreier, M.A. Sutton, Systematic errors in digital image correlation due to undermatched subset shape functions, Exp Mech 42(3) (2002) 303-310.
[39] J. Hiller, P. Hornberger, Measurement accuracy in X-ray computed tomography metrology: Toward a systematic analysis of interference effects in tomographic imaging, Precision Engineering 45 (2016) 18-32.
[40] D. Texier, J.-C. Stinville, M.P. Echlin, S. Pierret, P. Villechaise, T.M. Pollock, J. Cormier, Short crack propagation from cracked non-metallic inclusions in a Ni-based polycrystalline superalloy, Acta Materialia 165 (2019) 241-258.
[41] A. Bergsmo, F.P.E. Dunne, Competing mechanisms of particle fracture, decohesion and slip-driven fatigue crack nucleation in a PM nickel superalloy, International Journal of Fatigue 135 (2020) 105573.
[42] B. Larrouy, P. Villechaise, J. Cormier, O. Berteaux, Grain boundary-slip bands interactions: Impact on the fatigue crack initiation in a polycrystalline forged Ni-based superalloy, Acta Materialia 99 (2015) 325-336.
[43] S.W. Chen, C. Zhang, Z.X. Xia, H. Ishikawa, Z.G. Yang, Precipitation behavior of Fe2Nb Laves phase on grain boundaries in austenitic heat resistant steels, Materials Science and Engineering: A 616 (2014) 183-188.
[44] K. Suzuki, M. Koyama, S. Hamada, K. Tsuzaki, H. Noguchi, Planar slip-driven fatigue crack initiation and propagation in an equiatomic CrMnFeCoNi high-entropy alloy, International Journal of Fatigue 133 (2020) 105418.
[45] T.C. Lindley, G. Oates, C.E. Richards, A critical of carbide cracking mechanisms in ferride/carbide aggregates, Acta Metallurgica 18(11) (1970) 1127-1136.
[46] A. Kelly, The Strengthening of Metals by Dispersed Particles, Proceedings of The Royal Society A: Mathematical, Physical and Engineering Sciences 282 (1964) 63-79.

[47] S.H. Goods, L.M. Brown, Overview No. 1: The nucleation of cavities by plastic deformation, Acta Metallurgica 27(1) (1979) 1-15.
[48] M. Hassanipour, S. Watanabe, K. Hirayama, H. Toda, K. Uesugi, A. Takeuchi, Short crack growth behavior and its transitional interaction with 3D microstructure in Ti-6Al-4V, Materials Science and Engineering: A 738 (2018) 229-237.